

Stopping and reversing sound via dynamic dispersion tuning

Pragalv Karki^{1,*} and Jayson Paulose^{1,2,†}

¹*Department of Physics and Institute for Fundamental Science, University of Oregon, Eugene, OR 97403, USA*

²*Material Science Institute, University of Oregon, Eugene, OR 97403, USA*

Slowing down, stopping, and reversing a signal is a core functionality for information processing. Here, we show that this functionality can be realized by tuning the dispersion of a periodic system through a dispersionless, or flat, band. Specifically, we propose a new class of phononic metamaterials based on plate resonators, in which the phonon band dispersion can be changed from an acoustic to an optical character by modulating a uniform prestress. The switch is enabled by the change in sign of an effective coupling between fundamental modes, which generically leads to a nearly dispersion-free band at the transition point. We demonstrate how adiabatic tuning of the band dispersion can immobilize and reverse the propagation of a sound pulse in simulations of a one-dimensional resonator chain. Our study relies on the basic principles of thin-plate elasticity independently of any specific material, making our results applicable across varied length scales and experimental platforms. More broadly, our approach could be replicated for signal manipulation in photonic metamaterials and electronic heterostructures.

The tunability of sound transport properties after fabrication is a prominent feature underlying the appeal of phononic metamaterials [1]. In periodic structures, tunability can be achieved by modifying the band structure of vibrational excitations, which determines both the frequency ranges of sound insulation (via bandgaps) and the group velocity of sound propagation (via the frequency-momentum relationship or dispersion relation). Metamaterials with tunable phononic bands have been proposed which use modulation methods as varied as buckling [2, 3], large structural deformations [4–6], electrical [7–9] and optical [10] actuation, and prestress modulation [11–15]. While most of these proposals have targeted the tuning of bandgaps, several works [6–8, 14] have highlighted the ability to change group velocities by tuning the dispersion relation as a promising direction for metamaterials design.

In this work, we demonstrate how to stop and reverse signals in a tunable metamaterial by changing the dispersion character of an entire band. Specifically, we describe a physical mechanism to flip the sign of the group velocity across all quasimomenta (i.e., wavevectors associated with the excitations of the periodic lattice), thereby reversing the propagation direction of wave pulses (Fig. 1). At the point of sign switching, the group velocity vanishes throughout to create a flat phononic band which can localize and immobilize signals. Using full-wave finite element simulations, we show how adiabatic tuning of the dispersion allows us to store and reverse a sound pulse in a waveguide—a functionality which has potential applications in acoustic sensing [16, 17], signal processing [18], and computation [19–21].

We accomplish the desired change in dispersion by manipulating the coupling between adjacent degrees of freedom in a periodic structure. In our design, the relevant degrees of freedom are the fundamental (i.e., lowest-frequency) transverse vibrational modes of free-standing thin-plate mechanical resonators supported by a rigid

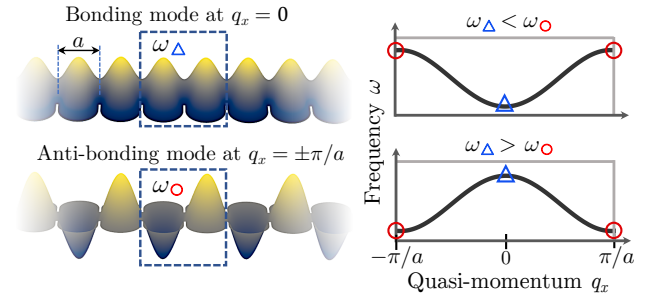


FIG. 1. Relationship between paired-mode frequencies and dispersion, illustrated for a periodic system with lattice constant a . *Left*, The Bloch mode of the lowest band at $q_x = 0$ is composed of a chain of in-phase or bonding pairs of fundamental excitations (top), whereas the mode at $q_x = \pm\pi/a$ is composed of out-of-phase or antibonding pairs (bottom). *Right*, Schematic of the different band dispersion relations when the frequency of the bonding pair ω_Δ is lower (top) or higher (bottom) than the antibonding pair frequency ω_\circ .

frame. However, the underlying physical principle is independent of the specific type of excitation, as illustrated in Fig. 1 for the lowest excitation band of coupled modes on an infinite periodic chain. In a tight-binding description of coupled excitations, the Bloch state at the band center (quasimomentum $q_x = 0$) is constructed from eigenmodes in a “bonding” configuration (adjacent eigenmodes are in-phase), while the state at the band edge ($q_x = \pm\pi/a$ where a is the lattice constant) is an assembly of out-of-phase or “antibonding” pairs. If the bonding state for a pair of building blocks is at a lower frequency than the antibonding one, the dispersion relation must increase from the band center to the band edge. In contrast, if the antibonding configuration has a lower frequency, the dispersion relation is a decreasing function of the quasimomentum magnitude. Therefore, flipping the bonding character of pairwise couplings across a periodic structure can reverse the group veloc-

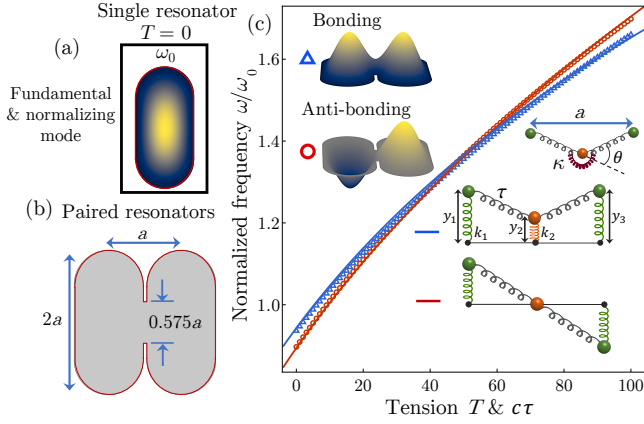


FIG. 2. (a) Geometry of a single resonator supported by a rigid boundary (red edge) and free to vibrate in the interior. Color intensity represents the displacement field of the fundamental mode at zero tension, whose frequency ω_0 is used as the normalizing frequency throughout the study. (b) Geometry of a resonator pair including the junction. This specific junction geometry was chosen to maximize mode separation at $T = 0$, but the effect persists for other narrow junctions. (c) Frequency of the two lowest eigenmodes of the resonator pair as a function of rescaled tension. Symbols are from finite-element simulations, and distinguish the bonding character of the corresponding eigenmode. Left inset shows numerically-determined eigenmodes at $T = 0$. Solid lines show lowest two eigenfrequencies of the discrete dynamical matrix, Eq. (2). Dimensionless parameters T (continuum model) and τ (discrete model) are related via $T = c\tau$, where $c = 47.5$ is a geometry-dependent linear mapping constant. Right inset shows tensile and torsional springs in the discrete model, and examples of bonding (blue) and antibonding (red) modes.

ity (the slope of the dispersion relation) throughout the band. Below, we show that the mechanics of thin plates under tension enables precisely such a reversal (Fig. 2). However, the approach could be replicated in other wave systems where the bonding character of paired degrees of freedom can be controlled, such as photonic crystals [22] or electronic heterostructures [23, 24].

Model of coupled plate resonators. Our starting point is the eigenvalue problem describing normal modes of the transverse displacement field $u(x, y)$ of an elastic plate resonator with bending modulus D , subjected to a uniform in-plane tension γ and clamped to a rigid plane curve along its edges [25]:

$$\begin{aligned} D\nabla^4 u_i - \gamma\nabla^2 u_i &= \rho\omega_i^2 u_i & \text{on domain } \Omega, \\ u_i &= \nabla u_i = 0 & \text{on boundary } \partial\Omega, \end{aligned} \quad (1)$$

where ρ is the mass per unit area and ω_i is the frequency of oscillation of the i th normal mode with displacement field $u_i(x, y)$. The clamped boundary condition captures the typical edge constraint for micromechanical resonators mounted on semiconductor substrates [26], but

our basic mechanism holds for Dirichlet boundary conditions as well [27]. Upon fixing the resonator geometry and choosing the width a as the distance unit, Eq. (1) has a single dimensionless parameter—the rescaled tension $T \equiv \gamma a^2/D$ [27]. While the bending modulus and density are materials properties, the tension is an externally-imposed stress which can be tuned through external manipulation (e.g. via laser heating [28] or electrostatic gating [8]). We use the fundamental mode with frequency ω_0 (Fig. 2(a)) as the basic degree of freedom in our system and consider the collective modes that arise upon coupling fundamental modes across multiple resonators through junctions as shown in Fig. 2(b).

For narrow junctions, the lowest two eigenmodes of a pair of resonators can be identified with a bonding and an antibonding configuration of the fundamental modes of the individual resonators (Fig. 2(c)). In the absence of a bending stiffness, Eq. (1) reduces to a Laplacian eigenfunction problem, for which the maximum principle dictates that the eigenfunction with the lowest eigenvalue must be of fixed sign over the domain. As a result, the bonding mode is guaranteed to be lower in frequency than the antibonding mode in the $D \rightarrow 0$, or $T \rightarrow \infty$, limit. However, the maximum principle does not hold for the *biharmonic* eigenfunction problem obtained in the $T \rightarrow 0$ limit of Eq. (1), for which domains with non-convex boundaries have been found to favor lowest-frequency eigenfunctions with sign changes within the domain [29, 30]. Therefore, we expect the antibonding mode to be at lower frequency when the external tension is set to zero, but to switch to higher frequency relative to the bonding mode at large tensions. Numerical solutions of the lowest two eigenmodes of the resonator pair, obtained via finite-element analysis [27], confirm this expectation (Fig. 2(c)). The lowest-frequency mode switches from antibonding to bonding type at a geometry-dependent threshold tension $T^* \approx 45$, at which the two lowest normal mode frequencies coincide to signify a degeneracy of the antibonding and bonding modes. The switch in bonding character also occurs for simply-supported edges (Dirichlet boundary conditions) [27].

Minimal model of mode-crossing mechanism. The balance between bending and tension which drives the eigenmode crossing can be captured in a simpler discrete model of coupled harmonic oscillators. The fundamental mode of an isolated resonator is modeled as a harmonic degree of freedom y confined to the vertical direction, with a unit mass and spring constant \tilde{k}_1 . Similar to past approaches [31], we then attempt to build the normal modes of coupled resonators by incorporating couplings among fundamental modes on adjacent oscillators, using e.g. a horizontal spring under tension. However, according to the von Neumann-Wigner theorem, coupling two degrees of freedom would generically create an *avoided* crossing of eigenvalues of the coupled system upon varying the coupling strength, in contrast to the observed

behavior in Fig. 2(c).

The key to obtaining the correct crossing behavior is to incorporate the plate deformation at the junction into the reduced description as an additional degree of freedom—specifically, a unit mass on a vertical spring with stiffness $\tilde{k}_2 > \tilde{k}_1$. This mass is coupled to the resonator degrees of freedom through tensed and torsional springs, as shown schematically in the right inset to Fig. 2(c). The coupling of the resonator modes due to tension is encoded in harmonic springs connecting each mode mass to the junction mass, which are prestressed with a tensile force $\tilde{\tau}$. These contribute a potential energy $U_s = \tilde{\tau}((y_1 - y_2)^2 + (y_2 - y_3)^2)/a$ to vertical displacements. The bending stiffness penalizes geometric curvature at the junction; we include this effect by defining a torsional spring which favors collinearity of the two tensile springs with associated harmonic energy $U_b = \tilde{\kappa}(1 - \cos \theta) \approx 2\tilde{\kappa}(y_1 - 2y_2 + y_3)^2/a^2$. By choosing ω_0^{-1} and a as the time and length units respectively, we obtain a discrete model with four dimensionless parameters k_1 , k_2 , τ , and κ [27] (the absence of the tilde indicates non-dimensionalized quantities). The non-dimensionalized stiffness matrix describing the dynamics of the three harmonic degrees of freedom is [27]

$$\mathbf{K} = \begin{pmatrix} k_1 + \tau + \kappa & -\tau - 2\kappa & \kappa \\ -\tau - 2\kappa & k_2 + 2\tau + 4\kappa & -\tau - 2\kappa \\ \kappa & -\tau - 2\kappa & k_1 + \tau + \kappa \end{pmatrix}. \quad (2)$$

The two lowest eigenfrequencies of the stiffness matrix correspond to the coupled modes that arise from weak-coupling of the fundamental modes [27]; the third mode is considerably higher in frequency and is not relevant to our analysis. When $\tau = 0$, the antibonding configuration has a lower frequency because the torsional spring remains undistorted (Fig. 2(c), lower right). Upon increasing τ with other parameters kept fixed, the bonding configuration becomes increasingly favored because it costs lower tensile energy, and the two modes become degenerate at $\tau = \sqrt{(3\kappa/2)^2 + \kappa(k_2 - k_1)} - 3\kappa/2$. If a linear relationship is assumed between the dimensionless tensions τ and T , the minimal model with four fit parameters quantitatively captures the evolution of the normal mode frequencies from the continuum model (compare symbols to solid lines in Fig. 2(c)).

Dispersion relation and flat band. To illustrate the consequences of the switch in parity of the lowest-frequency pair eigenmode on sound transport, we compute the mode spectrum for an infinite 1D chain of coupled resonators as a function of the quasimomentum q_x which indexes the Bloch eigenfunctions $u_{q_x}(x, y) = e^{iq_x x} \phi_{q_x}(x, y)$. For the continuum system, whose unit cell is depicted in Fig. 3(a), the numerically-determined spectrum [27] consists of infinitely many bands within the Brillouin zone $-\pi/a < q_x < \pi/a$, but the lowest band is built primarily from the fundamental modes

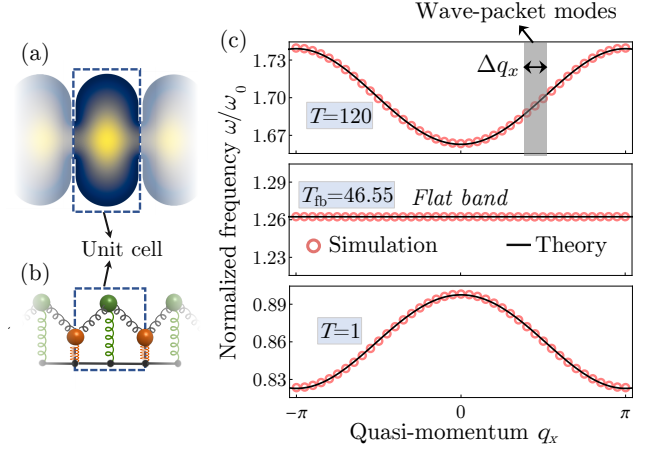


FIG. 3. Dispersion relation of the fundamental band. (a) Unit cell of the continuum model, with intensity variation representing the displacement of the Bloch eigenmode at $q_x = 0$ from finite-element calculations. (b) Unit cell of the discrete model. (c) Band structures of the continuum model at three values of rescaled tension (symbols), compared to bands computed from the discrete model (solid lines). Fit parameters τ and k_1 for different tensions T are: $T = 1 \rightarrow \{\tau, k_1\} \approx \{0.3195, 0.0381\}$, $T = 46.55 \equiv T_{fb} \rightarrow \{\tau, k_1\} \approx \{0.5217, 0.5502\}$, and $T = 120 \rightarrow \{\tau, k_1\} \approx \{0.7677, 1.4888\}$. Shaded region shows the quasimomentum range used to create the Gaussian wavepacket for the dynamical simulation.

of the individual resonators. The dispersion relation $\omega(q_x)$ for this band is captured in the reduced description with a two-mass unit cell shown in Fig. 3(b). The Fourier-transformed stiffness matrix obtained by upgrading Eq. (2) to a periodic chain is

$$\mathbf{K}(q_x) = \begin{pmatrix} a + b \cos q_x & -c(1 + e^{-iq_x}) \\ -c(1 + e^{iq_x}) & d \end{pmatrix}, \quad (3)$$

where $a = k_1 + 2\tau + 2\kappa$, $b = 2\kappa$, $c = \tau + 2\kappa$, and $d = k_2 + 2\tau + 4\kappa$. The frequency bands are then solved via $|\mathbf{K}(q_x) - \omega(q_x)^2 \mathbf{I}| = 0$.

Dispersion relations for the lowest band, computed using both the continuum and the discrete descriptions, are shown in Fig. 3(c) for three values of the globally-applied plate tension. Changing free parameters τ and k_1 in the discrete model effectively captures the changing of T in the continuum model [27]. We find that the band changes from optical type (frequency decreasing with quasimomentum) to acoustic type (frequency increasing with quasimomentum) as the tension is increased, in line with our expectation (Fig. 1). At a special value of the rescaled tension, the band becomes nearly dispersion-free, or flat. In the discrete model, we analytically establish the existence of a band with $\partial\omega/\partial q_x = 0$ throughout the Brillouin zone when $\tau = \sqrt{(2\kappa)^2 + \kappa(k_2 - k_1)} - 2\kappa$ [27], so a tension value leading to a perfectly flat band can always be found provided $k_2 > k_1$. In the continuum model, the dispersion does

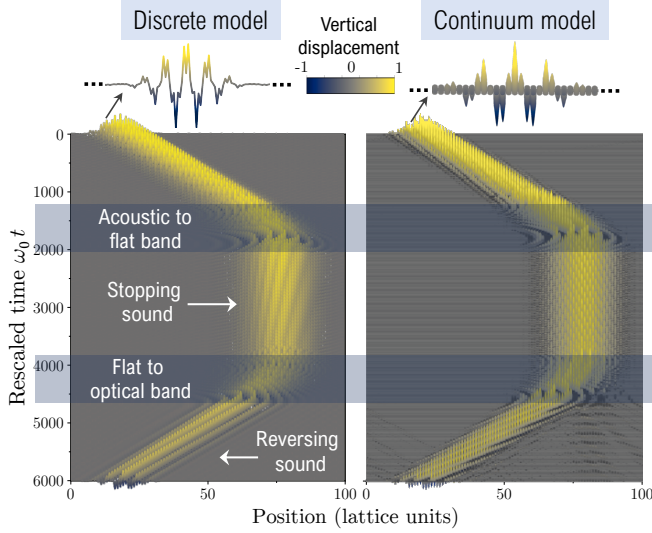


FIG. 4. Sound pulse reversal through dynamic dispersal tuning. Color map shows the vertical displacement evolution of Gaussian wavepackets in dynamical simulations of a linear chain of coupled resonators, for both the discrete (left) and the continuum (right) models. Initial pulses are shown for both systems at the top. Time advances from top to bottom; horizontal axis is position along the chain. Shaded time intervals are periods during which the dispersion was varied along a linear ramp connecting initial to final parameter values as described in the text.

not completely vanish; however, the bandwidth is limited to $10^{-3}\%$ of the mean band frequency. This minute deviation from a perfectly flat band can be reproduced in the discrete model by adding one more torsional spring to the unit cell, centered on the resonator mass [27].

Slowing, stopping, and reversing a sound pulse. As a prototypical example of manipulating a signal by dynamically tuning the dispersion through a flat band, we consider the evolution of a Gaussian wavepacket under uniform adiabatic modulation of the global tension in a resonator array. We performed full-wave simulations of the continuum model via a finite-element method, and classical dynamics simulations of the discrete mass-spring model via the velocity Verlet algorithm [27]. For both models, a 1D array of 100 unit cells was initialized with a wavepacket built from the band corresponding to $T = 120$ in Fig. 4. The Bloch eigenfunctions ϕ_{q_x} were used to construct a sound pulse using the equation

$$\mathbf{u}(n, t) = \sum_{q_x} \phi_{q_x} e^{i(q_x n - \omega(q_x)t)} e^{-\left(\frac{q_x - q_0}{\Delta q_x}\right)^2}, \quad (4)$$

where $\mathbf{u}(n, t)$ is the vector of displacements of the n th unit cell at time t , and the sum is over all allowed discrete quasimomenta q_x . In the discrete model, ϕ_{q_x} and \mathbf{u} are 2-vectors, while in the continuum model their length is determined by the mesh size of the finite-element dis-

cretization. The pulse was initialized at $t = 0$ with plane-wave weights centered at $q_0 = 1.2$ with normal deviation $\Delta q_x = 0.25$ (shaded region in Fig. 3(c)). The resulting pulse profile is localized to roughly 50 unit cells.

The subsequent evolution of the sound pulse is shown in Fig. 4 which tracks the instantaneous position along the chain as a function of time. During the evolution, the dispersion is dynamically tuned at two separate intervals (shaded regions in Fig. 4) by varying T in the continuum model and the parameters $\{\tau, k_1\}$ in the discrete model. Outside these intervals, the effective tension T is maintained at the constant values depicted in Fig. 3(c). At $T = 120$, the wavepacket has a positive group velocity (positive slope of the dispersion relation at q_0), and travels to the right (Fig. 4, top). The tension was then reduced over roughly 600 oscillation cycles towards the value $T = T_{fb}$ with zero group velocity (upper shaded region in Fig. 4). The slow modulation arrests the pulse, which oscillates in place with minimal distortion when the tension is maintained at T_{fb} (Fig. 4, middle). Finally, the tension was reduced further to $T = 1$ at which the wavepacket group velocity is negative (Fig. 3(c), bottom panel); this change reverses the propagation direction of the pulse (Fig. 4, bottom).

To approximate unavoidable losses in real systems, the simulations reported in Fig. 4 included linear drag forces which recreate a quality factor (Q-factor) of $Q \approx 6500$ [27]. While the energy density of the pulse decays as a result, the damping does not significantly distort the pulse profile or interfere with the expected zero group velocity (in contrast to metamaterials which attempt to generate a vanishing group velocity via local resonances [32]). Quality factors of order 10^4 are well within achievable limits for plate resonators as discussed below. The dynamic tuning could also be executed over fewer oscillations in a system with lower Q , at the cost of increased energy leakage into spurious modes.

Practical realizations. Experimental implementations of our proposal would require plate resonator arrays with high quality factors and tunable in-plane tension. Micromechanical systems based on two-dimensional materials are a prime candidate [8, 33]. The membranes are suspended over voids fabricated in semiconductor substrates with the desired metamaterial geometry, and the boundaries are restricted by adhesion of the membrane to the semiconductor at the void boundaries. Prestress modulation of phonon bands via electrostatic backgating has been demonstrated in SiN resonator arrays with $Q \approx 1,700$ [8], and Q-factors as high as 10^8 have been reported for individual SiN resonators [34]. Graphene-based resonator arrays [33] can be tuned via electrostatic [35] or thermally-induced [28] prestresses; Q-factors of order 10^5 have been reported [36, 37].

Future directions. Besides enabling signal reversal through dynamic dispersion tuning, the physical mechanism reported here also provides a means to realiz-

ing flat bands. Like their counterparts in electronics [38] and photonics [39], phononic flat bands [31, 40–42] are expected to have interesting transport, localization, and topological properties. Our design, which is a phononic analog of recipes for designing isolated electronic [43] and photonic [44] flat bands, can be extended to two-dimensional arrays and combined with lattice-based strategies to generate additional classes of flat bands [43, 45]. Although we focused on slow parameter modulation in this work, faster dynamic modulation of prestresses could enable non-Hermitian and active topological phenomena [46–49]. Discoveries of such phenomena could be aided by the analytically-tractable discrete model which quantitatively reproduces the numerically-solved continuum dynamics (Fig. 4). Beyond elasticity, modifying the bonding character of paired degrees of freedom has also been demonstrated in photonics [22], quantum dots [23], and superconductors [50], and has been proposed as a band-tuning mechanism for ultracold atoms [24]. Our basic approach, summarized in Fig. 1, could be explored in these systems as a route to tunable dispersion and controlled manipulation of photonic and electronic wavepackets.

Acknowledgments. We thank Benjamín Alemán, Andrew Blaikie, Brittany Carter, and David Miller for inspiration and input on experimental realizations; and Eric Corwin for useful comments. We acknowledge support from the College of Arts and Sciences at the University of Oregon via startup funds to JP.

* pragalvk@uoregon.edu

† jpaulose@uoregon.edu

- [1] Y.-F. Wang, Y.-Z. Wang, B. Wu, W. Chen, and Y.-S. Wang, *Applied Mechanics Reviews* **72** (2020), 10.1115/1.4046222.
- [2] P. Wang, F. Casadei, S. Shan, J. C. Weaver, and K. Bertoldi, *Physical Review Letters* **113**, 014301 (2014).
- [3] K. Bertoldi, *Annual Review of Materials Research* **47**, 51 (2017).
- [4] S. Babae, N. Viard, P. Wang, N. X. Fang, and K. Bertoldi, *Advanced Materials* **28**, 1631 (2016).
- [5] S. Hedayatrasa, K. Abhary, M. S. Uddin, and J. K. Guest, *Smart Materials and Structures* **25**, 055025 (2016).
- [6] R. K. Pal, J. Rimoli, and M. Ruzzene, *Smart Materials and Structures* **25**, 054010 (2016).
- [7] F. Casadei, T. Delpero, A. Bergamini, P. Ermanni, and M. Ruzzene, *Journal of Applied Physics* **112**, 064902 (2012).
- [8] J. Cha and C. Daraio, *Nature Nanotechnology* **13**, 1016 (2018).
- [9] K. Yi, M. Ouisse, E. Sadoulet-Reboul, and G. Matten, *Smart Materials and Structures* **28**, 065025 (2019).
- [10] N. Swintek, P. Lucas, and P. A. Deymier, *AIP Advances* **4**, 124603 (2014).
- [11] R. Feng and K. Liu, *Physica B: Condensed Matter* **407**, 2032 (2012).
- [12] E. G. Barnwell, W. J. Parnell, and I. D. Abrahams, *Extreme Mechanics Letters* **12**, 23 (2017).
- [13] A. O. Krushynska, A. Amendola, F. Bosia, C. Daraio, N. M. Pugno, and F. Fraternali, *New Journal of Physics* **20**, 073051 (2018).
- [14] R. K. Pal, M. Ruzzene, and J. J. Rimoli, *Extreme Mechanics Letters* **22**, 149 (2018).
- [15] Z.-N. Li, Y.-Z. Wang, and Y.-S. Wang, *International Journal of Solids and Structures* **182-183**, 218 (2020).
- [16] M. Fatemi and J. F. Greenleaf, *Science* **280**, 82 (1998).
- [17] Y. Q. Fu, J. Luo, N.-T. Nguyen, A. Walton, A. J. Flewitt, X.-T. Zu, Y. Li, G. McHale, A. Matthews, E. Iborra, *et al.*, *Progress in Materials Science* **89**, 31 (2017).
- [18] A. A. Oliner, ed., *Acoustic surface waves*, Topics in Applied Physics, Vol. 24 (Springer, 1978).
- [19] F. Li, P. Anzel, J. Yang, P. G. Kevrekidis, and C. Daraio, *Nature Communications* **5**, 5311 (2014).
- [20] F. Zangeneh-Nejad and R. Fleury, *New Journal of Physics* **20**, 073001 (2018).
- [21] Y. Wang, J.-p. Xia, H.-x. Sun, S.-q. Yuan, and X.-j. Liu, *Scientific Reports* **9**, 8355 (2019).
- [22] N. Caselli, F. Intonti, F. Riboli, A. Vinattieri, D. Gerace, L. Balet, L. H. Li, M. Francardi, A. Gerardino, A. Fiore, and M. Gurioli, *Physical Review B* **86**, 035133 (2012).
- [23] A. I. Yakimov, A. A. Bloshkin, and A. V. Dvurechenskii, *Semiconductor Science and Technology* **24**, 095002 (2009).
- [24] A. V. Zampetaki, J. Stockhofe, and P. Schmelcher, *Phys. Rev. A* **91**, 023409 (2015).
- [25] S. Timoshenko and S. Woinowsky-Krieger, *Theory of Plates and Shells*, Engineering Mechanics Series (McGraw-Hill, 1959).
- [26] P.-L. Yu, T. P. Purdy, and C. A. Regal, *Physical Review Letters* **108**, 083603 (2012).
- [27] See Supplementary Information for additional details of the discrete and continuum models, simulation methods, and fitting procedures for the discrete model parameters.
- [28] A. Blaikie, D. Miller, and B. J. Alemán, *Nature Communications* **10**, 1 (2019).
- [29] G. Sweers, *Electronic Journal of Differential Equations (EJDE)* [electronic only] **2001**, 285 (2001).
- [30] B. M. Brown, E. B. Davies, P. K. Jimack, and M. D. Mihajlović, “On the accurate finite element solution of a class of fourth order eigenvalue problems,” (1999), arXiv:math/9905038 [math.SP].
- [31] K. H. Matlack, M. Serra-Garcia, A. Palermo, S. D. Huber, and C. Daraio, *Nature Materials* **17**, 323 (2018).
- [32] G. Theocharis, O. Richoux, V. R. García, A. Merkel, and V. Tournat, *New Journal of Physics* **16**, 093017 (2014).
- [33] A. M. v. d. Zande, R. A. Barton, J. S. Alden, C. S. Ruiz-Vargas, W. S. Whitney, P. H. Q. Pham, J. Park, J. M. Parpia, H. G. Craighead, and P. L. McEuen, *Nano Letters*, *Nano Letters* **10**, 4869 (2010).
- [34] M. Yuan, M. A. Cohen, and G. A. Steele, *Applied Physics Letters* **107**, 263501 (2015), <https://doi.org/10.1063/1.4938747>.
- [35] T. Mei, J. Lee, Y. Xu, and P. X.-L. Feng, *Micromachines* **9**, 312 (2018).
- [36] J. Güttinger, A. Noury, P. Weber, A. M. Eriksson, C. Lagoin, J. Moser, C. Eichler, A. Wallraff, A. Isaacson, and A. Bachtold, *Nature Nanotechnology* **12**, 631 (2017).

- [37] M. Will, M. Hamer, M. Müller, A. Noury, P. Weber, A. Bachtold, R. V. Gorbachev, C. Stampfer, and J. Güttinger, *Nano Letters*, Nano Letters **17**, 5950 (2017).
- [38] O. Derzhko, J. Richter, and M. Maksymenko, *International Journal of Modern Physics B* **29**, 1530007 (2015).
- [39] D. Leykam and S. Flach, *APL Photonics* **3**, 070901 (2018).
- [40] S. Wu and J. Mei, *AIP Advances* **6**, 015204 (2016), <https://doi.org/10.1063/1.4939847>.
- [41] H. Zhu and F. Semperlotti, *Phys. Rev. Applied* **8**, 064031 (2017).
- [42] B. Li, Z. Li, J. Christensen, and K. T. Tan, *Applied Physics Letters* **114**, 081906 (2019), <https://doi.org/10.1063/1.5085782>.
- [43] T. Misumi and H. Aoki, *Phys. Rev. B* **96**, 155137 (2017).
- [44] W. Maimaiti, *Physical Review B* **95** (2017), 10.1103/PhysRevB.95.115135.
- [45] J.-W. Rhim and B.-J. Yang, *Phys. Rev. B* **99**, 045107 (2019).
- [46] R. Fleury, A. B. Khanikaev, and A. Alù, *Nature Communications* **7**, 11744 (2016).
- [47] H. Nassar, H. Chen, A. N. Norris, and G. L. Huang, *Phys. Rev. B* **97**, 014305 (2018).
- [48] F. Zangeneh-Nejad and R. Fleury, *Reviews in Physics* **4**, 100031 (2019).
- [49] C. Scheibner, W. T. M. Irvine, and V. Vitelli, *Physical Review Letters* **125**, 118001 (2020).
- [50] J. D. Pillet, V. Benzoni, J. Griesmar, J. L. Smirr, and Ç. Ö. Girit, *Nano Letters*, Nano Letters **19**, 7138 (2019).

Supplementary Information

Finite-element analysis of continuum model

To perform finite-element simulations without making explicit choices for the physical dimensions and materials parameters, we non-dimensionalize the continuum plate equation (Eq. (1) of the main text) using appropriate length and time scales. When the spatial coordinates are rescaled by the lattice constant a , the eigenmode equation becomes

$$\bar{\nabla}^4 u_i - \frac{\gamma a^2}{D} \bar{\nabla}^2 u_i = \frac{\rho a^4 \omega_i^2}{D} u_i,$$

where the bar represents gradients computed using the rescaled coordinates x/a and y/a . Therefore, when the geometry of the domain is prescribed as a plane curve in rescaled coordinates $(x/a, y/a)$, the eigenmodes are dependent only on the dimensionless parameter $T \equiv \gamma a^2/D$ which quantifies the size of the global tension. The eigenvalue problem whose solution provides the desired normal modes reduces to

$$\bar{\nabla}^4 u_i - T \bar{\nabla}^2 u_i = \lambda_i u_i,$$

where the eigenvalues λ_i are related to the physical mode frequencies ω_i via $\lambda_i = a^4 \rho \omega_i^2/D$. In the remainder of this section, we drop the bar for clarity; the variables

x and y and the gradient operator ∇ are understood to refer to the rescaled coordinates.

Finite-element analyses were done in the commercially available package COMSOL Multiphysics. The *general form pde* module was used to define an eigenvalue problem based on a fourth order partial differential equation describing thin plate elasticity,

$$\nabla \cdot \left[(u_{xxx} + 2u_{xyy} - Tu_x) \hat{x} + (u_{yyy} - Tu_y) \hat{y} \right] = \lambda u, \quad (5)$$

where subscripts denote partial derivatives of u with respect to those coordinates. The Dirichlet boundary condition $u = 0$ and Neumann boundary conditions $u_x = u_y = 0$ satisfy the clamped boundary condition. Simplifying the equation (5) gives $\nabla^4 u - T \nabla^2 u = \lambda u$, which is the desired eigenvalue problem. The simulation methods were tested by comparing numerically-derived eigensolutions for the square Laplacian plate (setting $D \rightarrow 0$) and circular clamped biharmonic plate (setting $T \rightarrow 0$) to known analytical results.

The continuum thin-plate resonator model has infinitely many bands, of which a subset are obtained numerically. In Fig. 5, the first eight bands and the eigenfunctions associated with those bands are shown as an example. In this study, we focused solely on the the lowest band, which is built primarily from the lowest-frequency, or fundamental, modes of individual resonators. This is apparent from the mode shape of the Bloch eigenfunction in Fig. 5(b), which mirrors the mode shape of the single-resonator fundamental mode.

We note here that the lowest frequency in the periodic system does not go to zero at $q_x = 0$ or $q_x = \pi$, i.e. a low-frequency bandgap exists in the resonator system. This bandgap is a consequence of the finite frequency of the fundamental mode. When the tension is set to zero, the vibrational frequency of a continuum displacement field scales as $\sqrt{D/(\rho l^4)}$ where l is the shortest length scale of variations of the displacement field. For a single resonator, l is at most some fraction of a and the fundamental frequency is of order $\sqrt{D/(\rho a^2)}$ with a prefactor larger than one [numerically, we find $\omega_0 \approx 27.3 \sqrt{D/(\rho a^2)}$, consistent with the apparent variation of the displacement field which happens over roughly a third of the resonator width in Figure 1(a)]. For an infinite 1D chain of resonators, the lowest frequency remains of order ω_0 because the narrow junctions only weakly perturb the adjacent modes and the displacement fields are still restricted by the resonator width a . If we were to widen the junctions, the lowest frequency of the band would drop, but it would still be bounded from below by the resonator height, $l \lesssim 2a \Rightarrow \omega \gtrsim 4 \sqrt{D/(\rho a^2)}$ and a finite bandgap is always expected. By contrast, for a two-dimensional resonator array we could nearly eliminate the bandgap by widening the coupling junctions in both directions. In that case, the vibrational response of

the lowest-frequency Bloch mode would approach that of a square plate of infinite dimension, which truly goes to zero as $l \rightarrow \infty$.

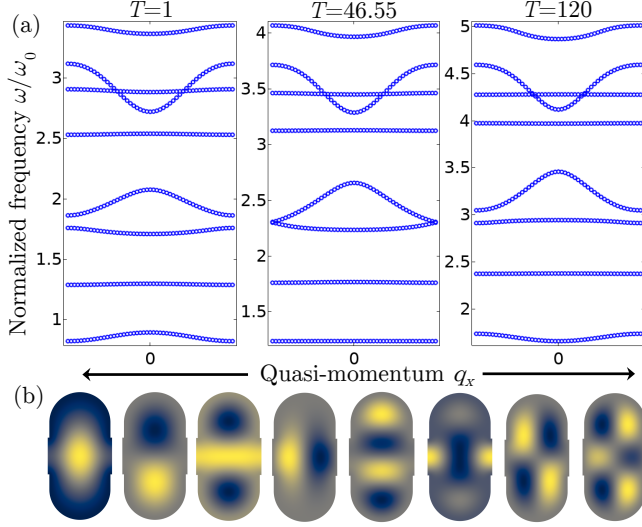


FIG. 5. Eight frequency bands (a) and their eigenfunctions (b) for three different tension T values. The change in the dispersive character of the first band intermediated by a flat band can be seen with increasing tension. Displacements in the second and fifth mode (b) can be seen to be isolated from neighboring resonators resulting in mostly non-dispersive bands (a) throughout different tension values. The third and fourth modes have band touching at corners of the Brillouin zone at the flat band tension $T = 46.55$ suggesting possible band inversion. The sixth and seventh modes have band crossing and the eighth mode simply changes its band width with increasing tension.

Insensitivity to boundary conditions

The bonding and anti-bonding mode flipping mechanism is insensitive to whether the domain boundary is clamped or simply supported (Dirichlet boundary condition only). In Fig. 6, the flipping mechanism is shown for the simply supported case for two different tension values, $T = 1$ and $T = 120$.

Having a junction between the resonators is more important than details of the boundary condition for the eigenmode switching. A clamped boundary condition was used in this study since that is the norm in experimental studies of membrane resonators.

Non-dimensionalization of discrete model

The Newtonian mechanics of the spring-mass chain, with all points assigned a mass m , is described by the

	Eigenmodes and normalized frequency	
	1 st Mode	2 nd Mode
$T=1$	0.91 	0.95
$T=120$	1.76 	1.81

FIG. 6. Eigenmodes and normalized frequencies of paired resonators with simply supported boundaries. At $T = 1$, the system is in the bending dominated region and hence the anti-bonding mode has a lower energy and at $T = 120$ the system is in the tension dominated region where the bonding mode has a lower energy.

second order differential equation

$$m \frac{d^2 \mathbf{y}}{dt^2} + \beta \frac{d\mathbf{y}}{dt} + \tilde{\mathbf{K}} \mathbf{y} = 0, \quad (6)$$

where $\mathbf{y} = \{y_1, y_2, \dots\}$ is the vector of vertical displacements, and \mathbf{K} is the stiffness matrix incorporating the effect of the on-site, tensed, and torsional springs. For the three-site model in Fig. 2 of the main text, the stiffness matrix reads

$$\tilde{\mathbf{K}} = \begin{pmatrix} \tilde{k}_1 + \frac{\tilde{\tau}}{\ell} + \frac{\tilde{\kappa}}{\ell^2} & -\frac{\tilde{\tau}}{\ell} - \frac{2\tilde{\kappa}}{\ell^2} & -\frac{\tilde{\kappa}}{\ell^2} \\ -\frac{\tilde{\tau}}{\ell} - \frac{2\tilde{\kappa}}{\ell^2} & \tilde{k}_2 + \frac{2\tilde{\tau}}{\ell} + \frac{4\tilde{\kappa}}{\ell^2} & -\frac{\tilde{\tau}}{\ell} - \frac{2\tilde{\kappa}}{\ell^2} \\ \frac{\tilde{\kappa}}{\ell^2} & -\frac{\tilde{\tau}}{\ell} - \frac{2\tilde{\kappa}}{\ell^2} & \tilde{k}_1 + \frac{\tilde{\tau}}{\ell} + \frac{\tilde{\kappa}}{\ell^2} \end{pmatrix}, \quad (7)$$

where ℓ is the horizontal spacing between the masses. To build a discrete model with dimensionless parameters that can be related to the continuum system, we choose ω_0^{-1} and a as time and length units respectively. The distance between primary on-site degrees of freedom y_i and y_{i+2} is also set to be a , so that $\ell = a/2$. Upon defining the rescaled time $t = \omega_0 \tilde{t}$, spring stiffnesses $k_i = \tilde{k}_i / m \omega_0^2$, the tension $\tau = 2\tilde{\tau} / a m \omega_0^2$, and the torsional stiffness $\kappa = 4\tilde{\kappa} / a^2 m \omega_0^2$, we obtain the equation

$$\frac{d^2 \mathbf{y}}{dt^2} + 2\zeta \frac{d\mathbf{y}}{dt} + \mathbf{K} \mathbf{y} = 0, \quad (8)$$

where \mathbf{K} is the non-dimensionalized stiffness matrix reported in the main text, and $\zeta = \beta / (m \omega_0)$ is the damping ratio. The quality factor is given by $Q = 1/2\zeta$. All the parameters presented in the main text for the discrete model without the tilde symbol are non-dimensionalized versions.

Eigenvalues and eigenvectors of 3-site reduced model

The eigenfrequencies of the 3-site reduced model in Eq. (2) of the main text were solved via $|\mathbf{K} - \omega^2 \mathbf{I}| = 0$ as,

$$\begin{aligned}\omega_1^2 &= k_1 + \tau, \\ \omega_{2,3}^2 &= 3\alpha + k_1 + k_2 \pm \sqrt{9\alpha^2 + (k_2 - k_1)(2\alpha + k_2 - k_1)},\end{aligned}\quad (9)$$

where, $\alpha = \tau + 2\kappa$. The corresponding eigenvectors are visualized in Fig. 7. The first two modes can be interpreted as antibonding and bonding modes of the continuum system respectively. The third mode is considerably separated from the first two modes in frequency for the fit parameters obtained in the main text, and is not considered in this study.

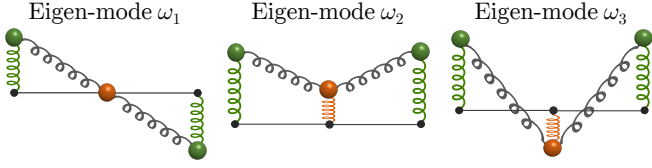


FIG. 7. Eigenmodes of the 3-site reduced model. In addition to the springs shown in this figure, torsional springs are also attached to the middle masses as shown in the bottom right inset of Fig. 2(c).

Deviation from perfectly flat band and additional bending stiffness

At the rescaled tension T_{fb} , the continuum model of the thin-plate resonator has a minute deviation from a perfectly flat band with bandwidth that is $10^{-3}\%$ of the mean band frequency (symbols in Fig. 8). For practical reasons and for demonstrating the tunable dispersion character of the fundamental band, such a small deviation is not consequential. However, even this variation can be incorporated in the discrete model by including an additional torsional spring, with rescaled stiffness κ' , centered on the resonator degree of freedom (green mass-springs in schematics). This addition modifies Eq. (3) as follows,

$$\mathbf{K}(q_x) = \begin{pmatrix} a + b \cos q_x & -c(1 + e^{-iq_x}) \\ -c(1 + e^{iq_x}) & d + e \cos q_x \end{pmatrix} \quad (10)$$

where $a = k_1 + 2\tau + 2\kappa + 4\kappa'$, $b = 2\kappa$, $c = \tau + 2\kappa + 2\kappa'$, $d = k_2 + 2\tau + 2\kappa' + 4\kappa$, and $e = 2\kappa'$.

Upon performing a fit with the additional parameter κ' , the deviation from the perfectly flat band is quantitatively recovered (dotted line in Fig. 8).

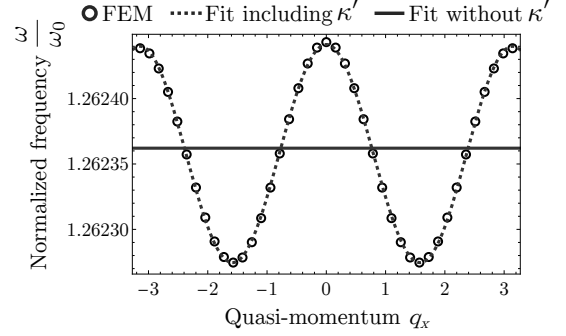


FIG. 8. Minute deviation from complete flatness. Fit functions are shown for the spring-mass model with bending stiffness κ only (solid line) at the junction point with the vertical spring stiffness k_2 and with additional bending stiffness κ' (dotted line) at the point with resonator stiffness k_1 .

Analytical derivation of flat band in discrete model

The existence of a perfectly flat band in the discrete model can be established provided $\kappa' = 0$. We start by assuming arbitrary κ and κ' , and find the normal mode frequencies of the dynamical matrix $\mathbf{K}(q_x)$ from equation (10) via $|\mathbf{K}(q_x) - \omega^2 \mathbf{I}| = 0$. This results in the quartic equation,

$$\begin{aligned}(\omega^2)^2 - \omega^2(a + b \cos q_x + d + e \cos q_x) \\ + (a + b \cos q_x)(d + e \cos q_x) - 2c^2(1 + \cos q_x) = 0.\end{aligned}\quad (11)$$

The coefficients of ω^2 and $\omega^0 = 1$ are minus the sum and the product of the two roots ω_1^2 and ω_2^2 respectively. If we require one of the roots to be a flat band, $\omega_1^2 = \alpha$ for some constant, then the other root must have the form

$$\omega_2^2 = \gamma + \delta \cos q_x + \phi \cos^2 q_x$$

to generate the requisite terms in the sum and product.

By matching coefficients of the $\cos q_x$ term and the remaining term in the sum and the product of the roots, we can find the relations between constants α , γ , δ , ϕ , and a , b , c , d , e , and eventually the spring stiffnesses k_1 , k_2 , τ , κ , κ' . We immediately find that one of b and e , i.e. one of the two bending stiffnesses, must be zero for the perfectly flat band to exist. Upon setting κ' to zero, the remaining parameters provide the band dispersion relations

$$\begin{aligned}\omega_1^2 &= 2\tau + k_1 \\ \omega_2^2 &= 2\tau + k_2 + 6\kappa + 2\kappa \cos q_x\end{aligned}\quad (12)$$

with the constraint

$$\tau = -2\kappa + \sqrt{(k_2 - k_1)\kappa + (2\kappa)^2}.\quad (13)$$

Note that this solution requires $k_2 > k_1$. However, as long as this condition is fulfilled, a tension τ can always be found to make the lower band completely flat.

The flat band is used to fit the band related to the fundamental mode from the continuum model at $T_{fb} = 46.55$. For tension values other than T_{fb} , the band is dispersive and must be fitted using the solution to the quartic equation Eq. (11).

Fitting procedure for reduced model parameters

Given our choice of physical units, the dimensionless parameters for the discrete model are fixed by fitting the eigenfrequencies of the discrete model to the dimensionless frequencies ω/ω_0 from the continuum finite-element analysis.

Three-site discrete model. For the analysis of the resonator pair (Fig. 2), we aimed to recover the change in frequency of the two lowest modes upon varying the prestress T in the continuum model by varying the tension τ in the reduced model, keeping all other dimensionless parameters fixed. While T and τ are related, they are different physical quantities (T is a force per unit length for the elastic plate, whereas τ is a tensile force on the horizontal springs). We assume a simple linear relation $T = c\tau$, where c is a constant parameter, and find that this relation is sufficient to recover the mode-crossing behavior.

Given the exact frequencies of the discrete model, Eq. (9), the parameter value $k_1 = 0.8000$ is fixed by equating it to the square of antibonding mode frequency from the continuum model at $T = \tau = 0$. The complete relationship between frequency and prestress (tension) for this mode is then quantitatively recovered by setting $c = 47.5$. Having set these two parameters, the remaining parameters $k_2 = 35$ and $\kappa = 0.0450$ were fixed by fitting the analytical form for ω_2 from Eq. (9) to the bonding mode frequency curve from the continuum model.

Band structure of infinite 1D chain. To obtain quantitative agreement of the discrete model with the continuum results, both τ and k_1 had to be changed with T . Physically, the need to modify k_1 reflects the fact that the bare resonator frequencies themselves depend on the prestress T in a nontrivial way that depends on geometry. Parameters $\kappa \approx 0.0575$ and $k_2 \approx 7.3724$ were fixed across all three prestress values, and parameters k_1 and τ were determined by fitting the analytical dispersion relation to that from the continuum model at each value of the prestress T . The resulting fit parameters for the three prestress values in Fig. 3 are: Flat band

parameters: $k_1 \approx 0.5502$ and $\tau \approx 0.5217$; Acoustic-like (top) band parameters: $k_1 \approx 1.4888$ and $\tau \approx 0.7677$; Optical-like (bottom) band parameters: $k_1 \approx 0.0381$ and $\tau \approx 0.3195$.

Dynamical simulations

Full-wave dynamical simulation was performed via finite element method in COMSOL for the following partial differential equation,

$$\frac{\partial^2 u}{\partial t^2} + 2\zeta \frac{\partial u}{\partial t} + \nabla^4 u - T \nabla^2 u = 0. \quad (14)$$

A predefined mesh in COMSOL called “Normal” calibrated for general physics was used for the full-wave dynamical simulation. Element size parameters for this mesh are as follows: maximum element size = 6.7, minimum element size = 0.03, maximum element growth rate = 1.3, curvature factor = 0.3, and resolution of narrow regions = 1. A time-dependent solver called the generalized alpha was used with a time-step of 0.01. A damping ratio of $\zeta \approx 8 \times 10^{-5}$ corresponding to a Q-factor $Q \approx 6500$ was used for the simulation.

Classical dynamical simulation of the discrete 1D spring-mass model was implemented in C++ using the velocity Verlet algorithm. The position and velocity were evolved with time iteration i as follows,

$$\begin{aligned} \mathbf{y}_{i+1} &+= \mathbf{v}_i \Delta t + \frac{1}{2} \mathbf{a}_i (\Delta t)^2 \\ \mathbf{v}_{i+1} &+= \frac{1}{2} (\mathbf{a}_{i+1} + \mathbf{a}_i) \Delta t, \end{aligned} \quad (15)$$

where, $+=$ is the increment operator in C language and $\mathbf{y} = \{y_1, y_2, \dots, y_n\}$, \mathbf{v} , and \mathbf{a} are the list of particle displacements in vertical direction, velocities, and accelerations respectively. The acceleration a_n at lattice site n is

$$\begin{aligned} a_n &= \frac{1}{m} \left[(\tau + 2\kappa)(y_{n+1} + y_{n-1}) - \kappa(y_{n+2} + y_{n-2}) \right. \\ &\quad \left. - (k_1 + 2\tau + 2\kappa)y_n - 2\zeta v_n \right], \text{ for even } n \\ \text{and, } a_n &= \frac{1}{m} \left[(\tau + 2\kappa)(y_{n+1} + y_{n-1}) \right. \\ &\quad \left. - (k_2 + 4\tau + 8\kappa)y_n - 2\zeta v_n \right], \text{ for odd } n, \end{aligned} \quad (16)$$

based on the dynamical matrix in the equation (3). A time-step $\Delta t = 0.01$ and a damping ratio $\zeta \approx 8 \times 10^{-5}$ were used for the simulation.